

Finding-Aware Anatomical Tokens for Chest X-Ray Automated Reporting

Francesco Dalla Serra^{1,2}, Chaoyang Wang¹, Fani Deligianni²,
Jeffrey Dalton², and Alison Q. O’Neil^{1,3}

¹ Canon Medical Research Europe, Edinburgh, United Kingdom
`francesco.dallaserra@mre.medical.canon`

² University of Glasgow, Glasgow, United Kingdom

³ University of Edinburgh, Edinburgh, United Kingdom

Abstract. The task of radiology reporting comprises describing and interpreting the medical findings in radiographic images, including description of their location and appearance. Automated approaches to radiology reporting require the image to be encoded into a suitable token representation for input to the language model. Previous methods commonly use convolutional neural networks to encode an image into a series of *image-level* feature map representations. However, the generated reports often exhibit realistic style but imperfect accuracy. Inspired by recent works for image captioning in the general domain in which each visual token corresponds to an object detected in an image, we investigate whether using local tokens corresponding to anatomical structures can improve the quality of the generated reports. We introduce a novel adaptation of Faster R-CNN in which *finding detection* is performed for the candidate bounding boxes extracted during anatomical structure localisation. We use the resulting bounding box feature representations as our set of *finding-aware* anatomical tokens. This encourages the extracted anatomical tokens to be informative about the findings they contain (required for the final task of radiology reporting). Evaluating on the MIMIC-CXR dataset [16, 17, 12] of chest X-Ray images, we show that task-aware anatomical tokens give state-of-the-art performance when integrated into an automated reporting pipeline, yielding generated reports with improved clinical accuracy.

Keywords: CXR · Automated Reporting · Anatomy Localisation · Findings Detection · Multimodal Transformer · Triples Representation

1 Introduction

A radiology report is a detailed text description and interpretation of the findings in a medical scan, including description of their anatomical location and appearance. For example, a Chest X-Ray (CXR) report may describe an opacity (a type of finding) in the left upper lung (the relevant anatomical location) which is diagnosed as a lung nodule (interpretation). The combination of a finding and its anatomical location influences both the diagnosis and the clinical

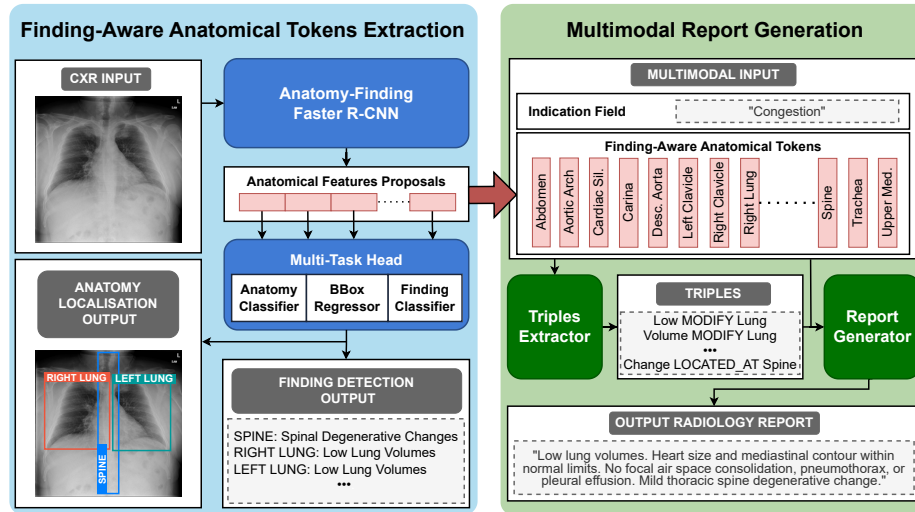


Fig. 1. Finding-aware anatomical tokens integrated into a multimodal CXR automated reporting pipeline. The CXR image and report are taken from the IU-Xray dataset [7].

treatment decision, since the same finding may have a different list of possible clinical diagnoses depending on the location.

Recent CXR automated reporting methods have adopted CNN-Transformer architectures, in which the CXR is encoded using Convolutional Neural Networks (CNNs) into global image-level features [13, 14] which are input to a Transformer language model [32] to generate the radiology report. However, the generated reports often exhibit realistic style but imperfect accuracy, for instance hallucinating additional findings or describing abnormal regions as normal. Inspired by recent image captioning works in the general domain [2, 19, 37] in which each visual token corresponds to an object detected in the input image, we investigate whether replacing the image-level tokens with local tokens – corresponding to anatomical structures – can improve the clinical accuracy of the generated reports. Our contributions are to:

1. Propose a novel multi-task Faster R-CNN [27] to extract *finding-aware anatomical tokens* by performing finding detection on the candidate bounding boxes identified during anatomical structure localisation. We ensure these tokens convey rich information by training the model on an extensive set of anatomy regions and associated findings from the Chest ImaGenome dataset [34, 12].
2. Integrate the extracted finding-aware anatomical tokens as the visual input in a state-of-the-art two-stage pipeline for radiology report generation [6]; this pipeline is multimodal, taking both image (CXR) and text (the corresponding text indication field) as inputs.
3. Demonstrate the benefit of using these tokens for CXR report generation through in-depth experiments on the MIMIC-CXR dataset.

2 Related Works

Automated Reporting Previous works on CXR automated reporting have examined the model architecture [5, 4], the use of additional loss functions [24], retrieval-based report generation [29, 10], and grounding report generation with structured knowledge [6, 35]. However, no specific focus has been given to the image encoding. Inspired by recent works in image captioning in the general domain [2, 19, 37], where each visual token corresponds to an object detected in an image, we propose to replace the image-level representations with local representations corresponding to anatomical structures detected in a CXR. To the best of our knowledge, only [33, 30] have considered anatomical feature representations for CXR automated reporting. In [33], they extract anatomical features from an object detection model trained solely on the anatomy localisation task. In [30], they train the object detector through multiple steps – anatomy localisation, binary abnormality classification and region selection – and feed each anatomical region individually to the language model to generate one sentence at a time. This approach makes the simplistic assumption that one anatomical region is described in exactly one report sentence.

Finding Detection Prior works have tackled the problem of finding detection in CXR images via weakly supervised approaches [36, 38]. However, the design of these approaches does not allow the extraction of anatomy-specific vector representations, making them unsuited for our purpose. Agu et al [1] proposed AnaXnet, comprising two modules trained independently: a standard Faster R-CNN trained to localise anatomical regions, and a Graph Convolutional Network (GCN) trained to classify the pathologies appearing in each anatomical region bounding box. This approach assumes that the finding information is present in the anatomical representations after the first stage of training.

3 Methods

We describe our method in two parts: (1) Finding-aware anatomical token extraction (Figure 1, left) – a custom Faster R-CNN which is trained to jointly perform *anatomy localisation* and *finding detection*; and (2) Multimodal report generation (Figure 1, right) – a two-step pipeline which is adapted to perform *triples extraction* and *report generation*, using the anatomical tokens extracted from the Faster R-CNN as the visual inputs for the multimodal Transformer backbone [32].

3.1 Finding-Aware Anatomical Token Extraction

Let us consider $A = \{a_n\}_{n=1}^N$ as the set of anatomical regions in a CXR and $F = \{f_m\}_{m=1}^M$ the set of findings we aim to detect. We define $f_{n,m} \in \{0, 1\}$ indicating the absence or presence of the finding f_m in the anatomical region a_n , and $f_n = \{f_{n,m}\}_{m=1}^M$ as the set of findings in a_n . We define *anatomy localisation*

as the task of predicting the top-left and bottom-right bounding box coordinates $c = (c_{x1}, c_{y1}, c_{x2}, c_{y2})$ of the anatomical regions A ; and *finding detection* as the task of predicting the findings f_n at each location a_n .

We frame anatomy localisation as a general object detection task, employing the Faster R-CNN framework to compute the coordinates of the bounding boxes and the anatomical labels assigned to each of them. First, the image features are extracted from the CNN backbone, composed of a ResNet-50 [13] and a Feature Pyramid Network (FPN) [22]. Second, the multi-scale image features extracted from the FPN are passed to the Region Proposal Network (RPN) to generate the bounding box coordinates $c_k = (c_{k,x1}, c_{k,y1}, c_{k,x2}, c_{k,y2})$ for each proposal k and to the Region of Interest (RoI) pooling layer, designed to extract the respective fixed-length vector representation $l_k \in \mathbb{R}^{1024}$. Each proposal’s local features l_k are then passed to a classification layer (*Anatomy Classifier*) to assign the anatomical label (a_k) and to a bounding box regressor layer to refine the coordinates. In parallel, we insert a multi-label classification head (*Findings Classifier*) – consisting of a single fully-connected layer with sigmoid activation functions – that classifies a set of findings for each proposal’s local features (see Appendix A).

During training, we use a multi-task loss comprising three terms: *anatomy classification loss*, *box regression loss*, and (multi-label) *finding classification loss*. Formally, for each predicted bounding box, this is computed as

$$\mathcal{L} = \mathcal{L}_{anatomy} + \mathcal{L}_{box} + \lambda \mathcal{L}_{finding}, \quad (1)$$

where $\mathcal{L}_{anatomy}$ and \mathcal{L}_{box} correspond to the anatomy classification loss and the bounding box regression loss described in [11] and $\mathcal{L}_{finding}$ is the finding classification loss that we introduce; λ is a balancing hyper-parameter set to $\lambda = 10^2$. We define

$$\mathcal{L}_{finding} = - \sum_{k=1}^K \sum_{m=1}^M w_m f_{k,m} \log(p_{k,m}) \quad (2)$$

a binary cross-entropy loss between the predicted probability $p_k = \{p_{k,m}\}_{m=1}^M$ of the k -th proposal and its associated ground truth $f_k = \{f_{k,m}\}_{m=1}^M$ (with $f_k = f_m$ if $a_k = a_m$). We class weight using $w_m = (1/\nu_m)^\alpha$, where ν_m is the frequency of the finding f_m in the training dataset and we empirically set α to 0.25.

At inference time, for each CXR image, we extract the finding-aware anatomical tokens $A_{tok} = \{l_n\}_{n=1}^N$, by selecting for each anatomical region the proposal with highest anatomical classification score and taking the associated latent vector representation l_n . Any non-detected regions are assigned a 1024-dimensional vector of zeros. A_{tok} is provided as input to the report generation model.

3.2 Multimodal Report Generation

We adopt the multimodal knowledge-grounded approach for automated reporting on CXR images as proposed in [6]. Firstly, *triples extraction* is performed to extract structured information from a CXR image in the form of triples, given

the indication field Ind as context. Secondly, *report generation* is performed to generate the radiology report from the triples with the CXR image and indication field again provided as context.

Each step is treated as a sequence-to-sequence task; for this purpose, the triples are concatenated into a single text sequence (in the order they appear in the ground truth report) separated by the special [SEP] token to form Trp , and the visual tokens are concatenated in a fixed order of anatomical regions. Two multimodal encoder-decoder Transformers are employed as the Triples Extractor (TE) and Report Generator (RG). The overall approach is:

$$\begin{aligned} \text{STEP 1} \quad & Trp = TE(seg_1 = A_{tok}, seg_2 = Ind) \\ \text{STEP 2} \quad & R = RG(seg_1 = A_{tok}, seg_2 = Ind \text{ [SEP] } Trp) \end{aligned} \quad (3)$$

where seg_1 and seg_2 are the two input segments which are themselves concatenated at the input. In step 2, the indication field and the triples are merged into a single sequence of text by concatenating them, separated by the special [SEP] token. Similarly to [8], the input to a Transformer corresponds to the sum of the textual and visual *token embeddings*, the *positional embeddings*—to inform about the order of the tokens—and the *segment embeddings*—to discriminate between the two modalities.

4 Experimental Setup

4.1 Datasets and Metrics

We base our experiments on two open-source CXR imaging datasets, Chest ImaGenome [34, 12] and MIMIC-CXR [16, 17, 12]. The MIMIC-CXR dataset comprises CXR image-report pairs and is used for the target task of report generation. The Chest ImaGenome dataset is derived from MIMIC-CXR, extended with additional automatically extracted annotations for 242,072 anteroposterior and posteroanterior CXR images, which we use to train the finding-aware anatomical token extractor. We follow the same train/validation/test split as proposed in the Chest ImaGenome dataset. We extract the *Findings* section of each report as the target text⁴. For the textual input, we extract the *Indication field* from each report.⁵ We annotate the ground truth triples for each image-report pair following a semi-automated pipeline using RadGraph [15] and sciSpaCy [25], as described in [6].

To assess the quality of the generated reports, we compute Natural Language Generation (NLG) metrics: BLEU [26], ROUGE [21] and METEOR [3]. We further compute Clinical Efficiency (CE) metrics by applying the CheXbert labeller [28] which extracts 14 findings to the ground truth and the generated reports, and evaluate F1, precision and recall scores. We repeat each experiment 3 times using different random seeds, reporting the average in our results.

⁴ https://github.com/MIT-LCP/mimic-cxr/blob/master/txt/create_section_files.py

⁵ https://github.com/jacenkow/mmbt/blob/main/tools/mimic_cxr_preprocess.py

4.2 Implementation

Finding-aware anatomical token extractor: We adapt the Faster R-CNN implementation from [20]⁶, by including the finding classifier. We initialise the network with weights pre-trained on the COCO dataset [23], then fine-tune it to localise 36 anatomical regions and to detect 71 findings within each region, as annotated in the Chest ImaGenome dataset (see Appendix C). The CXR images are re-sized by matching the shorter dimension to 512 pixels (maintaining the original aspect ratio) and cropping to a resolution of 512×512 (random crop during training and centre crop during inference). We train the model for 25 epochs with a learning rate of 10^{-3} , decayed every 5 epochs by a factor of 0.8. We select the model with the highest finding detection performances for the validation set, measured by computing the AUROC score for each finding at each anatomical region (see results in Appendix B).

Report generator: We implement a vanilla Transformer encoder-decoder at each step of the automated reporting pipeline. Both the encoder and the decoder consist of 3 attention layers, each composed of 8 heads and 512 hidden units. All the parameters are randomly initialised. We train step 1 for 40 epochs, with the learning rate set to 10^{-4} and we decay it by a factor of 0.8 every 3 epochs; and step 2 for 20 epochs, with the same learning rate as step 1. During training, we follow [6] in masking out a proportion of the ground-truth triples (50%, determined empirically), while during inference we use the triples extracted at step 1. We select the model with the highest CE-F1 score on the validation set.

Baselines We benchmark against other CXR automated reporting methods: R2Gen [5], R2GenCMN [4], \mathcal{M}^2 Tr.+fact_{ENTNLI} [24], CNN+Two-Step [6] and RGRG [30]. All these methods (except RGRG) adopt a CNN-Transformer and have shown state-of-the-art performances in report generation on the MIMIC-CXR dataset. All reported values are re-computed using the original code based on the same data split and image resolution as our method, except for [30] who already used this data split and image resolution, therefore we cite their reported results. We keep remaining hyperparameters as the originally reported values.

5 Results

Overall results In Table 1, we benchmark against other state-of-the-art CXR automated reporting methods and compare with the A_{tok} integrated into the full pipeline versus a simpler approach of the report generator model only, RG , which generates the report directly from image and indication field (omitting triples extraction). The proposed finding-aware anatomical tokens integrated with a knowledge-grounded pipeline [6] generate reports with state-of-the-art fluency (NLG metrics) and clinical accuracy (CE metrics). Moreover, the superior results of our $A_{tok} + RG$ approach compared to RGRG [30] suggests that providing the

⁶ https://pytorch.org/vision/main/models/generated/torchvision.models.detection.fasterrcnn_resnet50_fpn_v2.html

Table 1. Comparison of our proposed solution with previous approaches. TE = Triples Extractor, RG = Report Generator.

Method	NLG						CE		
	BL-1	BL-2	BL-3	BL-4	MTR	RG-L	F1	P	R
R2Gen [5]	0.381	0.248	0.174	0.130	0.152	0.314	0.431	0.511	0.395
R2GenCMN [4]	0.365	0.239	0.169	0.126	0.145	0.309	0.371	0.462	0.311
\mathcal{M}^2 Tr. + fact _{ENTNLI} [24]	0.402	0.261	0.183	0.136	0.158	0.300	0.458	0.540	0.404
ResNet-101 + TE + RG [6]	0.468	0.343	0.271	0.223	0.200	0.390	0.477	0.556	0.418
RGRG [30]	0.400	0.266	0.187	0.135	0.168	-	0.461	0.475	0.447
A_{tok} + RG (ours)	0.422	0.324	0.265	0.225	0.201	0.426	0.515	0.579	0.464
A_{tok} + TE + RG (ours)	0.490	0.363	0.288	0.237	0.213	0.406	0.537	0.585	0.496

Table 2. Comparison of different visual input representations (ResNet-101 vs. A_{tok}) using different pre-training supervision (ImageNet, Findings, Anatomy and Anatomy+Findings), integrated with the TE+RG two-step pipeline.

Visual Input	Supervision	NLG						CE		
		BL-1	BL-2	BL-3	BL-4	MTR	RG-L	F1	P	R
ResNet-101	ImageNet	0.468	0.343	0.271	0.223	0.200	0.390	0.477	0.556	0.418
ResNet-101	Findings	0.472	0.346	0.273	0.225	0.202	0.396	0.495	0.565	0.440
Naive A_{tok}	Anatomy	0.436	0.320	0.253	0.208	0.187	0.387	0.392	0.487	0.329
A_{tok}	Anatomy+Findings	0.490	0.363	0.288	0.237	0.213	0.406	0.537	0.585	0.496

GT Report	ResNet-101 + TE + RG	Naive A_{tok} + TE + RG	A_{tok} + TE + RG
The cardiac silhouette size is normal. There is mild calcification of the aortic knob. ¹ The mediastinal and hilar contours are within normal limits. The pulmonary vascularity is normal. Lungs are clear. No pleural effusion focal consolidation or pneumothorax is present. There are multilevel degenerative changes in the thoracic spine. ²	Heart size is normal. Atherosclerotic calcifications are noted at the aortic knob. ¹ Mediastinal and hilar contours are otherwise unremarkable. Mild atherosclerotic calcifications are noted at the aortic knob. ¹ Pulmonary vasculature is normal. Lungs are clear without focal consolidation. No pleural effusion or pneumothorax is present. There are no acute osseous abnormalities.	The heart size is normal. The mediastinal and hilar contours are unremarkable. The pulmonary vascularity is normal and the lungs are clear without focal consolidation. No pleural effusion or pneumothorax is present. There are mild degenerative changes in the thoracic spine. ²	The heart size is normal. The aorta is mildly tortuous with atherosclerotic calcifications noted at the aortic knob. ¹ The mediastinal and hilar contours are otherwise unremarkable and the pulmonary vascularity is not engorged. The lungs are clear without focal consolidation. No pleural effusion or pneumothorax is present. Mild degenerative changes are noted in the thoracic spine with mild loss of height of a mid thoracic vertebral body unchanged. ²

Fig. 2. Example report generated with different visual representations. The ground truth (GT) report (left) is followed by the generated reports using ResNet-101, naive anatomical tokens, and finding-aware anatomical tokens. Correctly detected findings are coloured green and errors are coloured red; we number corresponding descriptions.

full set of anatomical tokens together, instead of separately, gives better results. The broader visual context is indeed necessary when describing findings that span multiple regions *e.g.*, assessing the position of a tube.

Ablation Study Table 2 shows the results of adopting different visual representations. Firstly, we use a CNN (**ResNet-101**) trained end-to-end with *TE+RG* and initialised two ways: pre-trained on **ImageNet** versus pretrained on the **Findings** labels of Chest ImageGenome (details provided in Appendix D). Secondly, we extract anatomical tokens (A_{tok}) with different supervision of Faster R-CNN: anatomy localisation only (**Anatomy**) or anatomy localisation + finding detection (**Anatomy+Findings**). The results show the positive effect of

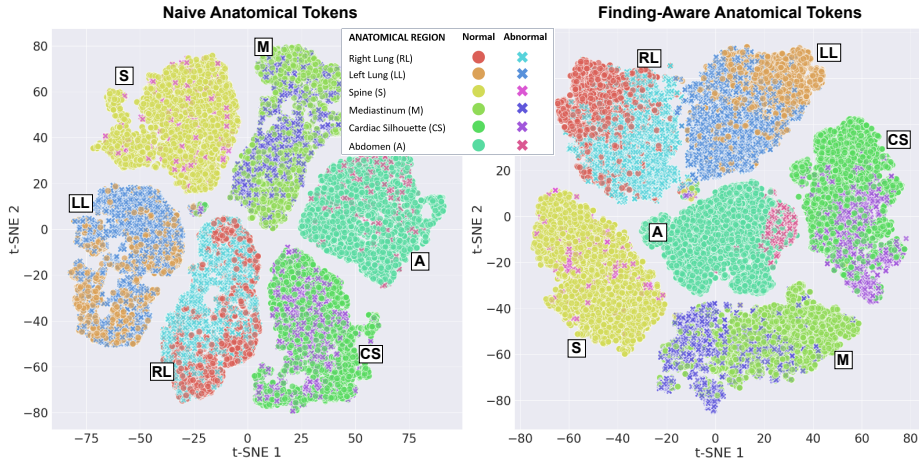


Fig. 3. T-SNE visualisation of normal and abnormal embeddings for a subset of visual tokens. Left: *naive anatomical token* embeddings extracted from Faster R-CNN trained solely on anatomy localisation. Right: *task-aware anatomical token* embeddings extracted from Faster R-CNN trained also on the finding detection task.

including supervision with finding detection either when pre-training ResNet-101 or as an additional task for Faster R-CNN. Example reports are shown in Figure 2 (abbreviated) and Appendix F (extended).

Anatomical Embedding Distributions In Figure 3, we visualise the impact of the finding detection task on the extracted anatomical tokens. To generate these plots, for 3000 randomly selected test set scans, we first perform principle component analysis [18] for dimensionality reduction of the token embeddings (from \mathbb{R}^{1024} to \mathbb{R}^{50}), then use t-distributed stochastic neighbour embedding (t-SNE) [31], colour coding the extracted embeddings by their anatomical region and additionally categorising as *normal* or *abnormal* (a token is considered abnormal if at least one of the 71 findings is positively labeled). For most anatomical regions, the normal and abnormal groups are better separated by the finding-aware tokens, suggesting these tokens successfully transmit information about findings. We also compute the mean distance between normal and abnormal clusters using Fréchet Distance (mFD) [9], measuring mFD=8.80 (naive anatomical tokens) and mFD=78.67 (finding-aware anatomical tokens).

6 Conclusion

This work explores how to extract and integrate anatomical visual representations with language models, targeting the task of automated radiology reporting. We propose a novel multi-task Faster R-CNN adaptation that performs finding detection jointly with anatomy localisation, to extract *finding-aware anatomical tokens*. We then integrate these tokens as the visual input for a multimodal

image+text report generation pipeline, showing that finding-aware anatomical tokens improve the fluency (NLG metrics) and clinical accuracy (CE metrics) of the generated reports, giving state-of-the-art results.

References

1. Agu, N.N., Wu, J.T., Chao, H., Lourentzou, I., Sharma, A., Moradi, M., Yan, P., Hender, J.: AnaXNet: Anatomy Aware Multi-label Finding Classification in Chest X-Ray. In: MICCAI (2021)
2. Anderson, P., He, X., Buehler, C., Teney, D., Johnson, M., Gould, S., Zhang, L.: Bottom-Up and Top-Down Attention for Image Captioning and Visual Question Answering. In: CVPR (2018)
3. Banerjee, S., Lavie, A.: METEOR: An automatic metric for MT evaluation with improved correlation with human judgments. In: ACL Workshop on Intrinsic and Extrinsic Evaluation Measures for Machine Translation and/or Summarization, pp. 65–72 (2005)
4. Chen, Z., Shen, Y., Song, Y., Wan, X.: Cross-modal Memory Networks for Radiology Report Generation. In: ACL-IJCNLP, pp. 5904–5914 (2021)
5. Chen, Z., Song, Y., Chang, T.-H., Wan, X.: Generating Radiology Reports via Memory-driven Transformer. In: EMNLP, pp. 1439–1449 (2020)
6. Dalla Serra, F., Clackett, W., MacKinnon, H., Wang, C., Deligianni, F., Dalton, J., O’Neil, A.Q.: Multimodal Generation of Radiology Reports using Knowledge-Grounded Extraction of Entities and Relations. In: AACL-IJCNLP, pp. 615–624 (2022)
7. Demner-Fushman, D., Kohli, M.D., Rosenman, M.B., Shooshan, S.E., Rodriguez, L.M., Antani, S., Thoma, G.R., McDonald, C.J.: Preparing a collection of radiology examinations for distribution and retrieval. *JAMIA* **23** **2**, 304–10 (2016)
8. Devlin, J., Chang, M.-W., Lee, K., Toutanova, K.: BERT: Pre-training of Deep Bidirectional Transformers for Language Understanding. In: NAACL, pp. 4171–4186. Association for Computational Linguistics (2019)
9. Dowson, D., Landau, B.: The Fréchet distance between multivariate normal distributions. *JMA* **12**(3), 450–455 (1982)
10. Endo, M., Krishnan, R., Krishna, V., Ng, A.Y., Rajpurkar, P.: Retrieval-Based Chest X-Ray Report Generation Using a Pre-trained Contrastive Language-Image Model. In: MLH, pp. 209–219 (2021)
11. Girshick, R.: Fast R-CNN. In: ICCV, pp. 1440–1448 (2015)
12. Goldberger, A.L. *et al.*: PhysioBank, PhysioToolkit, and PhysioNet: components of a new research resource for complex physiologic signals. *circulation* **101**(23), e215–e220 (2000)
13. He, K., Zhang, X., Ren, S., Sun, J.: Deep Residual Learning for Image Recognition. In: CVPR, pp. 770–778 (2016)
14. Huang, G., Liu, Z., Van Der Maaten, L., Weinberger, K.Q.: Densely Connected Convolutional Networks. In: CVPR, pp. 4700–4708 (2017)
15. Jain, S. *et al.*: RadGraph: Extracting Clinical Entities and Relations from Radiology Reports. In: NeurIPS: Datasets and Benchmarks Track (Round 1) (2021)
16. Johnson, A.E., Pollard, T.J., Berkowitz, S.J., Greenbaum, N.R., Lungren, M.P., Deng, C.-y., Mark, R.G., Horng, S.: MIMIC-CXR, a de-identified publicly available database of chest radiographs with free-text reports. *Scientific Data* **6**(1) (2019)

17. Johnson, A.E. *et al.*: MIMIC-CXR-JPG, a large publicly available database of labeled chest radiographs. arXiv preprint arXiv:1901.07042 (2019)
18. Jolliffe, I.: Principal component analysis. Springer Verlag, New York (2002)
19. Li, X. *et al.*: Oscar: Object-Semantics Aligned Pre-training for Vision-Language Tasks. In: ECCV, pp. 121–137 (2020)
20. Li, Y., Xie, S., Chen, X., Dollár, P., He, K., Girshick, R.: Benchmarking Detection Transfer Learning with Vision Transformers. arXiv preprint arXiv:2111.11429 (2021)
21. Lin, C.-Y.: ROUGE: A Package for Automatic Evaluation of Summaries. In: Text Summarization Branches Out, pp. 74–81 (2004)
22. Lin, T.-Y., Dollár, P., Girshick, R., He, K., Hariharan, B., Belongie, S.: Feature pyramid networks for object detection. In: CVPR, pp. 2117–2125 (2017)
23. Lin, T.-Y., Maire, M., Belongie, S., Hays, J., Perona, P., Ramanan, D., Dollár, P., Zitnick, C.L.: Microsoft COCO: common objects in context. In: ECCV (2014)
24. Miura, Y., Zhang, Y., Tsai, E., Langlotz, C., Jurafsky, D.: Improving Factual Completeness and Consistency of Image-to-Text Radiology Report Generation. In: NAACL, pp. 5288–5304 (2021)
25. Neumann, M., King, D., Beltagy, I., Ammar, W.: ScispaCy: Fast and Robust Models for Biomedical Natural Language Processing. In: BioNLP Workshop and Shared Task, pp. 319–327 (2019)
26. Papineni, K., Roukos, S., Ward, T., Zhu, W.-J.: BLEU: a Method for Automatic Evaluation of Machine Translation. In: ACL, pp. 311–318 (2002)
27. Ren, S., He, K., Girshick, R., Sun, J.: Faster R-CNN: Towards real-time object detection with region proposal networks. NIPS **28** (2015)
28. Smit, A., Jain, S., Rajpurkar, P., Pareek, A., Ng, A.Y., Lungren, M.: Combining Automatic Labelers and Expert Annotations for Accurate Radiology Report Labeling Using BERT. In: EMNLP, pp. 1500–1519 (2020)
29. Syeda-Mahmood, T. *et al.*: Chest X-ray Report Generation through Fine-Grained Label Learning. In: MICCAI, pp. 561–571 (2020)
30. Tanida, T., Müller, P., Kaissis, G., Rueckert, D.: Interactive and Explainable Region-guided Radiology Report Generation. In: CVPR, pp. 7433–7442 (2023)
31. Van der Maaten, L., Hinton, G.: Visualizing data using t-SNE. JMLR **9**(11) (2008)
32. Vaswani, A., Shazeer, N., Parmar, N., Uszkoreit, J., Jones, L., Gomez, A.N., Kaiser, L., Polosukhin, I.: Attention Is All You Need. NIPS **30** (2017)
33. Wang, Y., Wang, K., Liu, X., Gao, T., Zhang, J., Wang, G.: Self adaptive global-local feature enhancement for radiology report generation. arXiv preprint arXiv:2211.11380 (2022)
34. Wu, J.T. *et al.*: Chest ImaGenome Dataset for Clinical Reasoning. In: NeurIPS: Datasets and Benchmarks Track (Round 2) (2021)
35. Yang, S., Wu, X., Ge, S., Zhou, S.K., Xiao, L.: Knowledge Matters: Chest Radiology Report Generation with General and Specific Knowledge. MIA (2022)
36. Yu, K., Ghosh, S., Liu, Z., Deible, C., Batmanghelich, K.: Anatomy-Guided Weakly-Supervised Abnormality Localization in Chest X-rays. In: MICCAI (2022)
37. Zhang, P., Li, X., Hu, X., Yang, J., Zhang, L., Wang, L., Choi, Y., Gao, J.: VinVL: Revisiting Visual Representations in Vision-Language Models. In: CVPR, pp. 5579–5588 (2021)
38. Zhu, X., Pang, S., Zhang, X., Huang, J., Zhao, L., Tang, K., Feng, Q.: PCAN: Pixel-wise classification and attention network for thoracic disease classification and weakly supervised localization. CMIG **102**, 102137 (2022)

Supplementary Material

A Anatomy-Finding Faster R-CNN Architecture

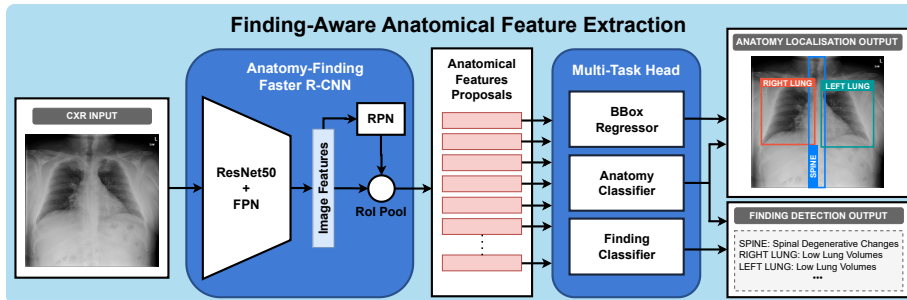


Fig. 4. The proposed anatomy-finding Faster R-CNN trained jointly on anatomy localisation and finding detection.

B Anatomy Localisation & Finding Detection Results

Table 3. Anatomy localisation and finding detection results of different configurations of the proposed Faster R-CNN: anatomy localisation only (Anatomy); and including the finding classification head (Finding) (*our proposed solution*).

Supervision		Anatomy Localisation	Finding Detection
Anatomy	Finding	mAP@0.5	AUROC
✓		0.938	-
✓	✓	0.918	0.863

We evaluate the anatomy localisation performance of our proposed Faster R-CNN by computing the mean Average Precision (mAP@0.5), with positive detections when the Intersection over Union score between the predicted bounding boxes and the ground truth is above 0.5. Finding detection performance is measured by computing the Area Under the Receiver Operating Characteristic (AUROC) for each finding at each anatomical region.

Table 3 shows that our proposed anatomy-finding Faster R-CNN performs worse than a standard Faster R-CNN trained solely on anatomy localisation

in terms of mAP@0.5 while achieving a good finding detection score. This is expected, as we select the best anatomy-only Faster R-CNN model based on the highest mAP@0.5 on the validation set and the anatomy-finding Faster R-CNN model based on the finding detection AUROC score. We observe that the trade-off between anatomy localisation and finding detection performance can be tuned by adjusting the weighting hyperparameter λ in the multi-task loss.

C Anatomical Regions & Findings

Table 4. Complete set of 36 anatomical regions and 71 findings used to supervise the anatomy localisation and the finding detection tasks, as annotated in the Chest ImaGenome dataset (<https://physionet.org/content/chest-imagenome/1.0.0/>).

Anatomical Regions			
abdomen	left clavicle	mediastinum	right lower lung zone
aortic arch	left costophrenic angle	right apical zone	right lung
cardiac silhouette	left hemidiaphragm	right atrium	right mid lung zone
carina	left hilar structures	right cardiac silhouette	right upper abdomen
cavoatrial junction	left lower lung zone	right cardiophrenic angle	right upper lung zone
descending aorta	left lung	right clavicle	spine
left apical zone	left mid lung zone	right costophrenic angle	svc
left cardiac silhouette	left upper abdomen	right hemidiaphragm	trachea
left cardiophrenic angle	left upper lung zone	right hilar structures	upper mediastinum
Findings			
airspace opacity	cyst/bulvae	linear/patchy atelectasis	pneumothorax
alveolar hemorrhage	diaphragmatic eventration (benign)	lobar/segmental collapse	prosthetic valve
aortic graft/repair	elevated hemidiaphragm	low lung volumes	pulmonary edema/hazy opacity
artifact	endotracheal tube	lung cancer	rotated
aspiration	enlarged cardiac silhouette	lung lesion	scoliosis
atelectasis	enlarged hilum	lung opacity	shoulder osteoarthritis
bone lesion	enteric tube	mass/nodule (not otherwise specified)	spinal degenerative changes
breast/nipple shadows	fluid overload/heart failure	mediastinal displacement	spinal fracture
bronchiectasis	goiter	mediastinal drain	sub-diaphragmatic air
cabg grafts	granulomatous disease	mediastinal widening	subclavian line
calcified nodule	hernia	multiple masses/nodules	superior mediastinal mass/enlargement
cardiac pacer and wires	hydropneumothorax	pericardial effusion	swan-ganz catheter
chest port	hyperaeration	picc	tortuous aorta
chest tube	ij line	pigtail catheter	tracheostomy tube
clavicle fracture	increased reticular markings/ild pattern	pleural effusion	vascular calcification
consolidation	infiltration	pleural/parenchymal scarring	vascular congestion
copd/emphysema	interstitial lung disease	pneumomediastinum	vascular redistribution
costophrenic angle blunting	intra-aortic balloon pump	pneumonia	

D CNN Pre-Training on Chest ImaGenome Findings

We train ResNet-101 on the set of 71 findings labels listed in Appendix C. Differently from Faster R-CNN, ResNet-101 is trained only to classify whether findings are present or absent in a CXR without any further anatomical localisation of each finding. We train ResNet-101 for 50 epochs, with an initial learning rate set to 10^{-3} and decrease every 2 epochs by a factor of 0.5. The loss term corresponds to a binary cross-entropy:

$$\mathcal{L}_{class} = - \sum_{m=1}^M w_m f_m \log(p_m)$$

between the predicted probability of each class p_m and the ground truth f_m . We class weight with $w_m = (1/\nu_m)^{0.25}$, where ν_m corresponds to the frequency of the finding f_m in the training set.

E Hyperparameter Search

Table 5. Hyperparameter search space. We highlight in **bold** the chosen values.

Model	Hyperparameter	Search Space
Anatomy-Finding Faster R-CNN	learning rate	{0.001, 0.0005, 0.0001 , 0.00005}
	λ	{1, 10, 100 , 1000}
	α	{0, 0.25 , 0.50, 0.75, 1}
Triples Extractor	learning rate	{0.0005, 0.0001 , 0.00005}
Report Generator	learning rate	{0.0005, 0.0001 , 0.00005}
	triples masking %	{30, 40, 50 , 60, 70}

F Example predicted reports

GT Report	ResNet-101 + TE + RG	Naive A _{tok} + TE + RG	A _{tok} + TE + RG
Cardiac size is top normal. Aside from atelectasis in the left base the lungs are clear. ¹ There is no pneumothorax or pleural effusion. There is hardware material in the cervical spine.	Cardiac mediastinal and hilar contours are normal. Pulmonary vasculature is normal. Lungs are clear without focal consolidation. No pleural effusion or pneumothorax is seen. There is no evidence of pulmonary edema. There is minimal atelectasis in the right mid lung. There is no evidence of pneumoperitoneum.	The cardiomeastinal and hilar contours are within normal limits. The lungs are well expanded and clear. There is no focal consolidation pleural effusion or pneumothorax. There is minimal left basilar atelectasis. ¹	There is mild left basilar atelectasis. ¹ No focal consolidation is seen. There is no pleural effusion or pneumothorax. The cardiac and mediastinal silhouettes are stable and unremarkable.
There is linear opacification of the left lung base ¹ and right mid lung likely representing atelectasis. ² The lungs are otherwise clear. The cardiac is top normal in size. There is no pleural effusion or pneumothorax.	Pa and lateral views of the chest provided.	Pa and lateral views of the chest provided. There is no focal consolidation effusion or pneumothorax. The cardiomeastinal silhouette is normal. Imaged osseous structures are intact. No free air below the right hemidiaphragm is seen.	A linear opacity at the left lung base is most consistent with subsegmental atelectasis. ^{1,2} The lungs are otherwise clear. No focal consolidation pulmonary edema pleural effusion or pneumothorax. The cardiomeastinal silhouette is normal. Imaged osseous structures are intact. No free air below the right hemidiaphragm is seen.
Left-sided pacemaker device is noted with leads terminating in the right atrium and right ventricle. ¹ Mild to moderate enlargement of cardiac silhouette is re-demonstrated. ² The mediastinal and hilar contours are unremarkable. Pulmonary vasculature is not engorged. Lungs are clear without focal consolidation. No pleural effusion or pneumothorax is present. There are no acute osseous abnormalities detected.	Left-sided pacemaker device is noted with leads terminating in the right atrium and right ventricle. ¹ Cardiac silhouette size is normal. The mediastinal and hilar contours are unremarkable. The pulmonary vasculature is normal. Lungs are clear without focal consolidation. No pleural effusion or pneumothorax is seen. There are no acute osseous abnormalities.	Heart size is normal. The mediastinal and hilar contours are normal. The pulmonary vasculature is normal. Lungs are clear without focal consolidation. No pleural effusion or pneumothorax is seen. There are no acute osseous abnormalities.	Left-sided dual-chamber pacemaker is noted with leads terminating in the right atrium and right ventricle. ¹ Heart size is mildly enlarged. ² Mediastinal and hilar contours are normal. Pulmonary vasculature is normal. Lungs are clear. No pleural effusion or pneumothorax is present. No acute osseous abnormalities detected.
As compared to the previous radiograph the patient has received a nasogastric tube. ¹ The course of the tube is unremarkable the tip of the tube projects over the middle parts of the stomach. ² There is no evidence of complications notably no pneumothorax. Left plate-like atelectasis. ³ No pleural effusions. No pneumonia no pulmonary edema.	As compared to the previous radiograph the patient has received a nasogastric tube. ¹ The course of the tube is unremarkable the tip of the tube projects over the middle parts of the stomach. ² There is no evidence of complications notably no pneumothorax.	As compared to the previous radiograph there is no relevant change. Low lung volumes. Borderline size of the cardiac silhouette with tortuosity of the thoracic aorta. No pulmonary edema. No pneumonia no pleural effusions. No pneumothorax.	A nasogastric tube terminates within the stomach. ^{1,2} The heart is normal in size. The mediastinal and hilar contours are normal. Plate-like atelectasis is present in the left mid lung. ³ There is no pleural effusion or pneumothorax.

Fig. 5. Examples of predicted reports with different visual representations (examples selected randomly from the subset of reports where predictions were different between representation methods). From left to right: the ground truth (GT) report, the predicted reports using a CNN, the naive anatomical tokens and the finding-aware anatomical tokens as the visual representations. In generated reports, correctly detected positive findings are highlighted in green, and errors are highlighted in red. The equivalent text spans in the ground truth report are also highlighted; we number corresponding descriptions.